ICONO 2001: Fundamental Aspects of Laser-Matter Interaction and Physics of Nanostructures (eds. A. V. Andreev et al.), Proc. SPIE, Vol. 4748 (2002) 476-485

Semiconductor Nanostructures for Quantum Wire Lasers

D. Piester, A. A. Ivanov, A. S. Bakin, H.-H. Wehmann, A. Schlachetzki

Institut für Halbleitertechnik, Technische Universität Carolo-Wilhelmina, P. O. Box 3329
D-38023 Braunschweig, Germany, iht@tu-bs.de

ABSTRACT

We report on the improvements of an InGaAs/InP quantum wire (QWR) laser leading to a new concept of a single QWR laser. Its index/gain guiding structure consists of a vertical waveguide in combination with a laterally patterned semi-insulating current blocking layer with an additional oxide layer, which is realized by a simple self-aligning sub-µm lithography step. A further improvement of the structure is possible by reducing the thickness of InP buffer layers, which were necessary due to technological reasons. One InP buffer layer may be omitted completely by increasing the growth temperature from 600 °C to 640 °C. By employing metal-organic vapor-phase epitaxy we found a significant increase of In-content of the QWRs at the raised temperature.

Keywords: nanostructures, quantum wires, quantum wells, semiconductor lasers, InGaAs, InP, V-groove, MOVPE, wet-chemical etching

1. INTRODUCTION

During the last decades semiconductor nanostructures developed into an intensively investigated field in physics as well as in engineering. The application of a quantum cascade laser demonstrated recently for spectroscopic trace-gas detection clearly shows the possibilities of "quantum engineering" with semiconductor nanostructures[1,2]. One reason for their significance is the possibility to determine the physical properties precisely by controlling the geometrical structure in the nanometer range. For example, by limiting the charge carrier motion at least in one dimension to the order of the de Broglie wavelength, quantization effects have drastic consequences on the density-of-state function. While in bulk crystals the density-of-states depends on the square root of the energy E of the carriers, it develops, after the step-like shape for two-dimensional structures (quantum well, QWL), $1/\sqrt{E}$ singularities at the bandedges of one-dimensional quantum wires (QWR)[3]. Thus, the energy distribution should be much narrower in the case of such QWRs than for bulk crystals. In the case of semiconductor laser applications we expect a significant reduction of the threshold current in comparison with common laser diodes[4], because a population inversion can be attained at lower pumping current due to the effective injection of charge carriers into a small energy interval. We also expect a reduction of the temperature dependence of the threshold current[5]. Lately it was shown by comparing QWL- with similarly fabricated QWR-lasers that the temperature dependence of the emission wavelength shift is indeed reduced for lower dimensionality[6]. Since the first observation of stimulated emission in QWRs by Kapon et al.[7] the physical and device properties were studied very intensively[8]. Until now, the lowest threshold current of 188 µA measured at room temperature is found by Tiwari et al.[9]. This was achieved by employing anisotropic growth on V-groove patterned GaAs-substrates with an InGaAs QWR. One crucial point for V-groove QWR lasers is the current confinement. Besides *pn*-junctions[10] or proton implantation[7] also oxide configurations are used[11]. The latter is arranged by a lithography method which removes parasitic quantum structures in order to improve the carrier capture efficiency of the QWRs[12]. The most promising material system for long-distance optical-fibre communications is InGaAsP-InP. While the wavelength range up to 1.3 µm can be covered also by GaAs-based devices, only In(Ga)As(P)-InP has been experimentally demonstrated for lasers in the 1.55 µm wavelength region[13,14].

In 1999, we reported on the fabrication and characterization of single InGaAs-InP QWRs[15]. They were grown in high quality V-grooves in InP substrates[16]. These QWRs were inserted into a laser structure as an active region[17]. Based on calculations, we optimized the design and the necessary technologies for its realization. The background of Fig. 1 is a scanning-electron microscopy (SEM) image (decorated in order to visualize the details of the cross-section of this QWR laser). On a highly *n*-doped InP substrate first an *n*-doped InGaAsP waveguiding layer with a bandgap-equivalent wavelength of 1.2 µm is grown, which is followed by a semi-insulating (s.i.) InP current blocking layer. After etching

V-grooves into this layer stack, the active layer of the laser is deposited, which forms the QWR in the tip of the V-groove. The growth is completed by a second quaternary layer to assist the optical confinement and a *p*-type InP layer with a *p*-InGaAs cap. Finally the structure is contacted by metallization. Laser action of the single InGaAs QWR was demonstrated, though an additional second laser line appeared in the electroluminescence (EL) spectra. However, the properties of the QWR laser alone were very promising[17].

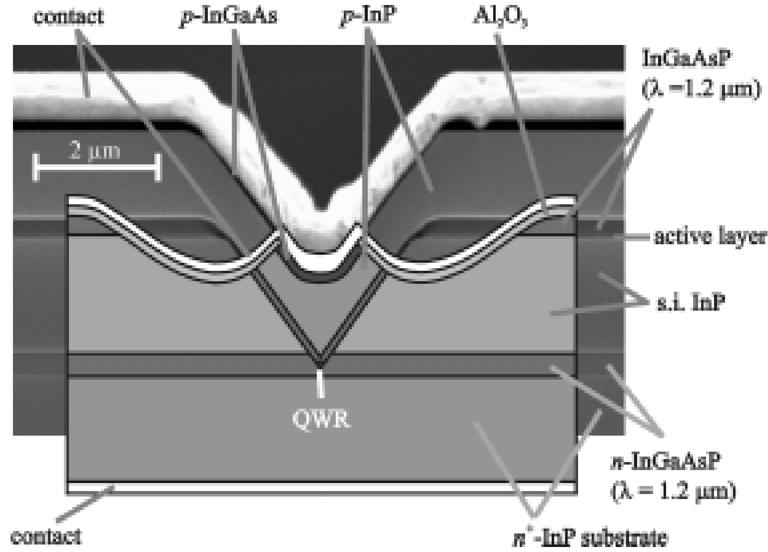

Figure 1. Concept of a single quantum wire laser with an index/gain guiding structure (foreground), and scanning-electron micrograph of a laser structure realized earlier (background).

In this article we present improvements of our concept leading to a single-QWR laser with an index/gain guiding structure which is shown schematically in the foreground of Fig. 1. It comprises an optimized active region. In addition, the current injection into the active region is enhanced by inserting an auxiliary Al_2O_3 current blocking layer after removing parasitic quantum structures which are responsible for the second laser line. We discuss the crucial quantities for the fabrication of QWRs, in particular the dimensions and material compositions of layers grown by metall-organic vapor-phase epitaxy (MOVPE) on V-groove patterned substrates. The device characteristics were analyzed by photoluminescence (PL). We present experimental results to improve the carrier injection into the active region. These investigations include the presentation of a self-aligning masking technique in the sub-µm regime using standard photolithography, results of growth experiments of QWRs at higher temperature, and tunneling with InGaAs-InP hetero-nanostructures.

2. BASIC TECHNOLOGIES

We first discuss the fabrication of quantum wires by employing anisotropic growth on V-groove patterned InP substrates using MOVPE. These structures are the essential parts of QWR lasers. We study the simplified layer sequence like that of Fig. 2 in order to derive important characteristics of the nanostructures found in our laser design. With a two-step anisotropic wet-chemical etching process V-grooves (typically 3 µm in width and distance) were structured in (100)-orientated InP substrates through a titanium film patterned by conventional photolithography and lift-off technique[16]. The V-grooves are aligned along $[0\bar{1}1]$-direction with {111}A-sidewalls. After carefully removing the Ti etching mask[18] the MOVPE growth is performed at 600 °C and total pressure of 100 hPa[15]. The epitaxial growth starts with an InP buffer layer for improved crystal quality, followed by a nominally lattice-matched $In_{1-x}Ga_xAs$ layer with $x = 0.47$. This ternary layer is covered by an InP cap layer. Due to the anisotropic growth of the ternary alloy, quantum structures with varying geometries and compositions appear. In Fig. 2 a schematic of the InGaAs QWLs and QWRs grown on V-groove patterned InP substrate is shown. We can distinguish four different quantum structures: the InGaAs QWR in the tip of each V-groove (I), the QWL on the unpatterned (100)-surface (II), and QWLs on the {111}-sidewalls (III), narrowing in the lower part in the vicinity of the QWR (IV). The QWRs were shown by transmission-electron microscopy[19] with the thickness t_I measured by atomic-force microscopy[20] (AFM). An example is

shown as the left inset in Fig. 2. The thicknesses of the QWLs t_{II} to t_{IV} were determined by SEM measurements[15] with a nominally 400 nm InGaAs layer grown on a V-grooved InP substrate (see central inset of Fig. 2). Additional AFM and PL investigations[15,19,21] (cf. right inset of Fig. 2) allow us to determine quantum-structure thicknesses and compositions (t_I to t_{IV} and x_I to x_{IV}, resp., cf. Fig. 2).

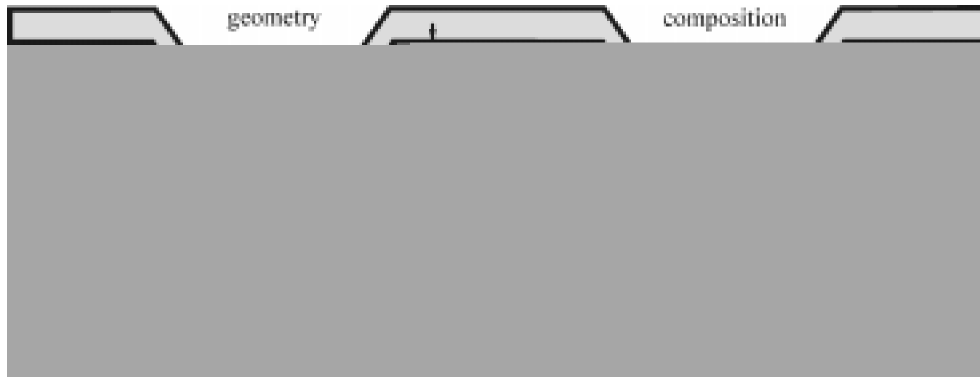

Figure 2. Schematic cross-section of the InGaAs quantum structure on an InP V-grooved substrate. Different quantum structures (I to IV) are indicated and the crucial parameters thickness (t_I to t_{IV}) and composition (x_I to x_{IV}) are labeled. Techniques applied to determine these parameters are shown as insets schematically.

If a QWL of a nominal thickness t_n with a Ga-content $x_n = 0.47$ (lattice matched to InP) is grown on an unpatterned planar InP substrate as specified, then we find for the QWR the thickness and composition values $t_I = 1.78 \cdot t_n$ and $x_I = 0.47 \pm 0.03$, respectively. The QWLs between the V-grooves are thicker than the nominal layer ($t_{II} = 1.23 \cdot t_n$) but Ga-rich ($x_{II} = 0.51$). At the same time the QWLs on the {111}-planes are significantly thinner with a very low Ga-content: $t_{III} = 0.34 \cdot t_n$, $t_{IV} = 0.16 \cdot t_n$, and $x_{III,IV} = 0.29$, respectively.

We incorporated the quantum structure as characterized in this manner into a laser structure. It consists of three layers grown in a first epitaxy step on n^+-doped InP substrate: 500 nm n^+-InP buffer layer, 400 nm n-InGaAsP waveguiding layer, and 1800 nm s.i.-InP current blocking layer (cf. Fig. 1). In Fig. 3 a) a SEM image of the cleaved mirror facet of a complete laser structure is shown (to achieve material contrast the cleaved surface was selectively etched[20]). After etching the V-groove with a tip-position exact in the middle of the quaternary layer[17], a second growth step of the active region follows, i.e. a thin InP buffer layer, which was deposited in order to enhance the quality of the following InGaAs-QWR, the QWR itself, and an additional thin InP-layer. This stabilizes the QWR during the heating phase from 600 °C to 640 °C, the growth temperature of the following nominally 200 nm thick InGaAsP-layer serving as a second waveguiding layer in order to optimize the optical filling factor. Finally a p-doped InP and a p^+-InGaAs layer were deposited, where the latter ensures an Ohmic contact. The e-beam evaporated metal contact was structured along the V-groove, which can be seen as a bright layer in Fig. 3 a). Finally, the sample is lapped down from the backside to about

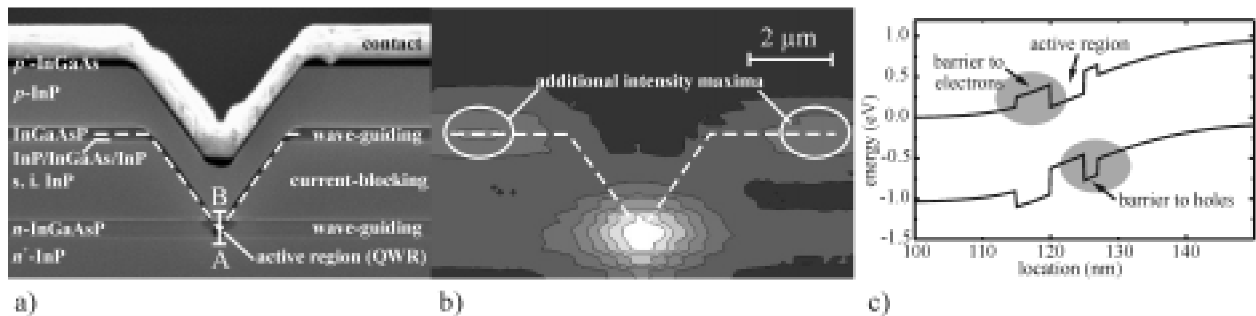

Figure 3. Structure and electroluminescence of a quantum wire laser as well as schematic bandedges in the active region: a) scanning-electron microphotograph of the cleaved mirror after material-selective etching, b) optical near field of the electroluminescence on the same scale (80 mA driving current at room temperature; the broken lines in a) and b) track the upper quaternary layer), c) schematic band diagram of the active region along line AB in a).

about 100 µm and contacted by metallization. The samples were cleaved into laser bars of about 1 mm resonator length. In order to determine the origin of the electrically induced optical radiation output we employ EL microscopy. The room-temperature EL (80 mA driving current) of a QWR laser structure is shown in Fig. 3 b). The highest intensity (bright spot in the centre of the picture) is located in the V-groove's tip. Additional maxima in the second waveguiding quaternary layer near the edges of the V-groove are visible. The upper quaternary layer is marked in Fig. 3 a) and b) by broken lines. The intensity of the satellite maxima is about one third of the main maximum. We attribute these spots to a parasitic laserdiode within the upper quaternary layer emitting at a wavelength of about 1.15 µm[17]. The intensity originating from the lower quaternary layer is only one tenth of the maximum intensity.

Figure 3 c) is an outline of the active region of our laser structure. The upper curve delineates the conduction band edge, the lower curve the valence band edge in thermodynamic equilibrium along the line AB in Fig. 3 a) through the QWR. In Fig. 3 c) the structure was grown during the first epitaxy step up to 115 nm. Only the upper part of the lower waveguiding layer is shown. In order to provide optimum growth conditions after V-groove etching, the second epitaxy starts with a 5 nm InP buffer layer, on which the InGaAs quantum wire layer of a few nm in thickness was deposited. This InP buffer layer, in the following called lower buffer layer, represents a barrier to electrons on foreward-bias condition. The upper InP buffer layer is deposited on the active region, with a thickness of 2 nm in this example. Thus we stabilize the QWR during heating from 600 °C, the optimized QWR growth temperature[22] to 640 °C, the optimized growth temperature of the quaternary layer beyond 127 nm. The hole injection can be impeded even by thin upper buffer layers. Despite these barriers our devices showed laser action at 15 K[17]. However, besides the QWR emission at 890 meV a second, parasitic laser line appeared at 1066 meV. Based on a two-diode model we derive a threshold current of 38 mA and a differential quantum efficiency of 98 % for the QWR laser. These promising data were the motivation for further optimization of the structure. We examine specific schemes to improve the current injection into the active region and to eliminate the parasitic InGaAsP laser.

3. DEVICE FABRICATION

In this section we describe the modified laser structure (cf. Fig. 1) and its fabrication technology. To this end we concentrate on the removal of the parasitic laser and an additional current blocking layer. For this we employ a self-aligning lithography technique[12], which enables us to reliably eliminate parasitic structures and to add an oxide current blocking layer[11] on the sub-µm scale. The necessary technological steps are condensed in Fig. 4. The V-grooved InP su6fbs- rpuree(b)-its the laser stce of98(Ft)-10gf.3wı˝[0(s-).d In fmi-2(stl ste p(h)7otoureist)-8at wi-2 thw-24e bol(edt(h)7iock73(
. d w n (
groov(w)299(nn)8(

Figure 5. Adjusting photoresist thickness in the V-groove tip by varying the exposure time; insets show SEM images of the V-groove in InP without (a) and with photoresist in the tip after a 90 s exposure (b).

The easiest way to eliminate the parasitic structures on the {111}- and (100)-facets is non-material-selective and isotropic etching. For this purpose we emplyed $HBr : CH_3COOH : K_2Cr_2O_7$[23] (BCK for short) with different compositions denoted in brackets. In order to achieve reproducible results solutions with an etching rate below 10 nm/s are preferable. Fig. 6 illustrates the optimization process. We start with the etching of InP by a composition of (2:2:1)[17]. The etching-rate is determined from the slope of the depth versus time dependence in the diffusion controlled regime, i.e. for times above 10 s (cf. an example as inset of Fig. 6). The higher etching-rate at the beginning is due to an initially reaction-limited process. This means that there is a minimum etching-depth (e.g. the extrapolated etching-depth d_0 in Fig. 6) below which the etching-rate ceases to be valid.

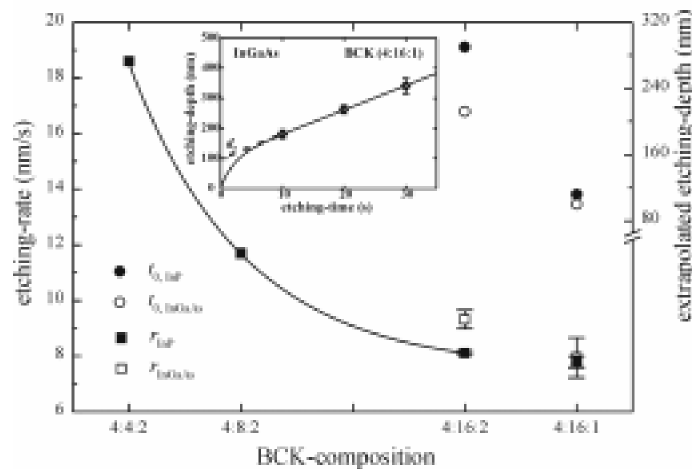

Figure 6. (100) etching-rates r of BCK with different compositions as determined from the constant slope of the respective depth-time dependences shown as inset. The extrapolated etching-depth d_0 is a lower boundary below which r loses its validity.

The etching-rate is reduced by increasing the acetic acid concentration, which only supplies H_3O^+-ions to adjust the pH-value without directly influencing the etching process itself. By increasing its concentration from 4 to 16 parts per volume the etching rate for (100) InP is reduced to about 8 nm/s. Applying this solution to InGaAs a slightly higher etching rate is observed due to a remaining week material-sensitive behavior. Because HBr selectively attacks InP (InGaAs is insensitive to HBr) the etching rate of the ternary alloy can be adjusted by the $K_2Cr_2O_7$-concentration. By

reducing its fraction from 2 to 1 the InGaAs etching-rate can be brought into line with that for InP. With a volume-ratio of (4:16:1) we found a solution which attacks InGaAs and InP with the same etching-rate.

In order to examine the etching behavior of the solution on a structured surface (cf. step b) in Fig. 4) we patterned an InP substrate with V-grooves and covered their tips according to Fig. 5 with photoresist. Afterwards the samples were etched in BCK (4:16:1) for 60 s, 100 s, and 150 s. The respective cross-sections are given as SEM images in Fig. 7 a) to c). The broken line in a) visualizes the geometry of the V-groove before its treatment. The resulting rounded surfaces with a maximum etching depth near the mask are due to the diffusion-limited, isotropic etching process. Thus it is obviously possible to remove the parasitic quantum structures next to the V-groove tip without affecting the structures itself. Furthermore, the undercut of the photoresist can be extended by increasing the etching time (cf. Fig. 7 a) to c)). With a minimum undercut of 300 nm a lift-off technique can be easily applied in order to form an additional current blocking layer next to the QWR. For this purpose 100 nm Al_2O_3 was electron-beam evaporated and the photoresist was dissolved in 1-methyl-2-pyrrolidone lifting the Al_2O_3-layer off the V-groove tip as shown in Fig. 7 d) (cf. Fig. 4 e) and foreground of Fig. 1).

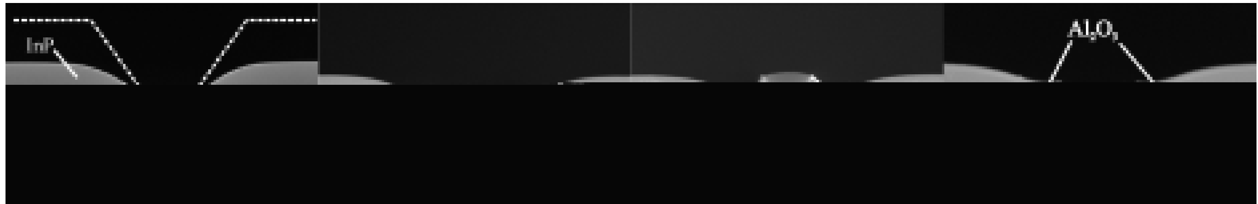

Figure 7. SEM images of V-grooves with covered tip after etching in BCK (4:16:1) for 60 s (a), 100 s (b), and 150 s (c); in d) the complete structure after 100 s etching time and after lift-off is shown.

4. EXPERIMENTAL RESULTS

As stated above, for an improved carrier injection into the QWR the upper buffer layer should be omitted. This entails the same growth temperature T_{growth} for the QWR and the following quaternary waveguiding layer. Therefore, we deposited the QWR structures of Fig. 2 at 640 °C and compared their PL appearance with structures grown at 600 °C (Fig. 8). All quantum structures contribute to the luminescence spectra according to their thicknesses, compositions, and

Figure 8. Normalized photoluminescence (PL) spectra of QWR samples grown at different temperatures: a) comparison between as grown and partly covered or partly removed surfaces, respectively; b) PL spectra of QWR samples.

effective area. However, the PL-signal of the (100) QWL (II in Fig. 2) dominates the spectra shown as dashed curves (as grown) in Fig. 8 a) for both growth temperatures. This dominance can be overcome either by covering the (100) surface with a Ti mask[15] (upper solid curve) or by applying the self-aligning lithography process with a subsequent BCK-etching step described in section 3 (lower solid curve in Fig. 8). In the first case, with Ti cover, signals of the remaining three quantum structures (I, III, and IV in Fig. 2) appear in the solid curve, whereas the BCK etching process

completely removes the contributions of the (100) QWL and the upper part of the (111) QWLs (II and III in Fig. 2) and – depending on the exposure and etching times – even the contribution of the lower part of the (111) QWL (IV).

We now discuss the clearly visible redshift of the QWR related peak (I) for the higher growth temperature. In order to quantify the redshift we compare the two spectra in Fig. 8 b) of layers, both grown at different temperatures under optimized conditions for nominally lattice-matched $In_{1-x}Ga_xAs$, i.e. $x = 0.47$. The PL spectrum of the "600 °C"-sample shows after Ti-evaporation two maxima at 0.916 eV and 1.007 eV, which are both related to {111} QWLs (III and IV in Fig. 2). The QWR peak (I) is visible as a shoulder at 0.857 eV. Its low intensity is the result of its small area with a width of a few tens of nanometer as compared to the width of QWLs which is in the range of microns. The "640 °C"-sample was prepared by the self-aligned etching technique leaving only the lower part of the {111} QWL ($E_{IV} = 1.099$ eV) and the QWR itself ($E_I = 0.819$ eV). Again, the redshift of the QWR related peak is clearly visible. Additionally, the peak (IV) shows a blueshift. If we assume, that the thicknesses of the quantum structures remain more or less unchanged, the shifts are related to changes in the InGaAs composition. Increasing the growth temperature leads to an In rich QWR and a Ga rich QWL (IV).

In Fig. 9 the results are summarized. The quantum-structure thickness dependence of the transition energies for optical experiments is calculated by solving Schrödinger's equation[15]. The horizontal dash-dotted line represents the expected PL energy E_G for bulk $In_{0.53}Ga_{0.47}As$ at 13 K. The transition energies for $In_{1-x}Ga_xAs$ QWRs of composition x in a range from 0.37 to 0.50 are given as the other solid curves. The dashed curves represent the calculations for QWLs of composition 0.47 and 0.29, respectively. The grey symbols are the results with quantum structures grown at 600 °C[15]. The solid squares represent QWRs where the error bars indicate the uncertainty of the AFM measurements. The transition energies obtained by conventional PL are marked as squares, by cathodoluminescence (CL) as rhomb and by micro PL as circles. The transition energies of the thin QWLs on the {111} planes are marked as upwards-pointing triangles for the upper (III) and downwards-pointing triangles for the lower (IV) part. The QWLs on the (100) surface and the QWR are nearly lattice matched, while the QWLs on the {111}-sidewalls are extremely Ga-poor. The latter was confirmed by AFM-investigations of selectively etched cleavage planes of InGaAs/InP heterostructures[21]. The black symbols mark the measured transition energies of layers grown at higher temperature (640 °C). The QWRs (black squares) with a nominal thickness of 12.5 nm are clearly below 804 meV, the expected energy of bulk InGaAs lattice matched to InP. This means, that the QWRs are Ga-poor in any case, irrespective of their thickness. On the other side, the {111} QWLs grown at 640 °C (black triangles) are more or less lattice matched and thus, contain more Ga as compared to their "600 °C"-counterparts. However, by reducing the In/Ga-ratio in the gasphase during the deposition, it is possible to shift the composition of the QWRs in a controlled manner towards lattice-matching (see arrow a) in Fig. 9).

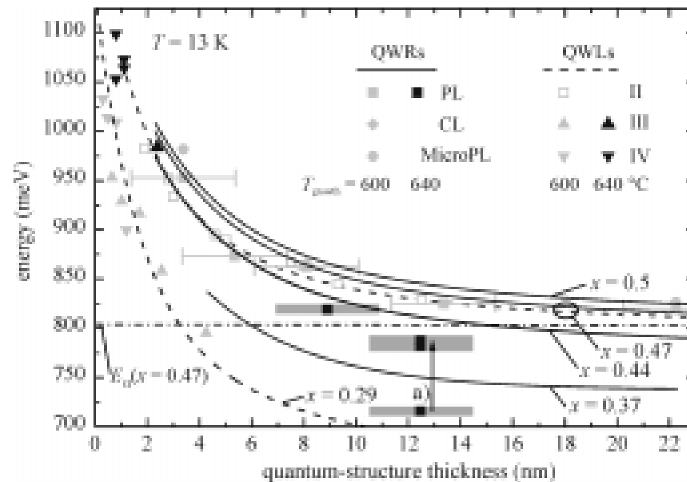

Figure 9. Determining of the InGaAs-InP quantum-structure composition.

Thus the upper InP buffer layer can be omitted by adjusting the growth temperature. In order to enhance the electron capture from the substrate into the active region, the lower InP buffer layer should be reduced in its thickness as much as possible to enable tunneling through the potential barrier (cf. Fig. 3 c)). But, a minimum thickness should be retained in order to prevent defect generation during the growth of the QWR layer directly on the etched surface of the V-

groove. From this point of view the optimum buffer layer thickness should be between 5 and 50 nm, respectively[18]. A trade-off between layer quality – i.e. a thick buffer – and effective electron tunneling – i.e. a thin buffer – is found by a study of the tunneling current through InP-barriers surrounded by InGaAs. If the barrier thickness is varied, the influence on the tunneling current becomes visible. We examined barrier thicknesses from 50 nm down to 1.5 nm. The epitaxial layers were grown on n^+-doped InP substrate by MOVPE using the same growth conditions as in the case of the other QWR layers, i. e. 20 hPa and 640 °C. The samples consist of a highly Si-doped InP buffer followed by 200 nm n^+-InGaAs (both $N_D \approx 2\times10^{18}\,\mathrm{cm}^{-3}$). The following 580 nm thick undoped InGaAs reduces the background doping concentration at the bottom of the barrier. The structure is completed by a 40 nm undoped InGaAs spacer and 600 nm n^+-InGaAs. Ohmic contacts are formed by electron-beam deposited Ti-AuGe-Au. By means of standard photolithography, about 150-µm-diameter circular mesas are etched by BCK. Finally, Ti-AuGe-Au is deposited on the backside of the samples.

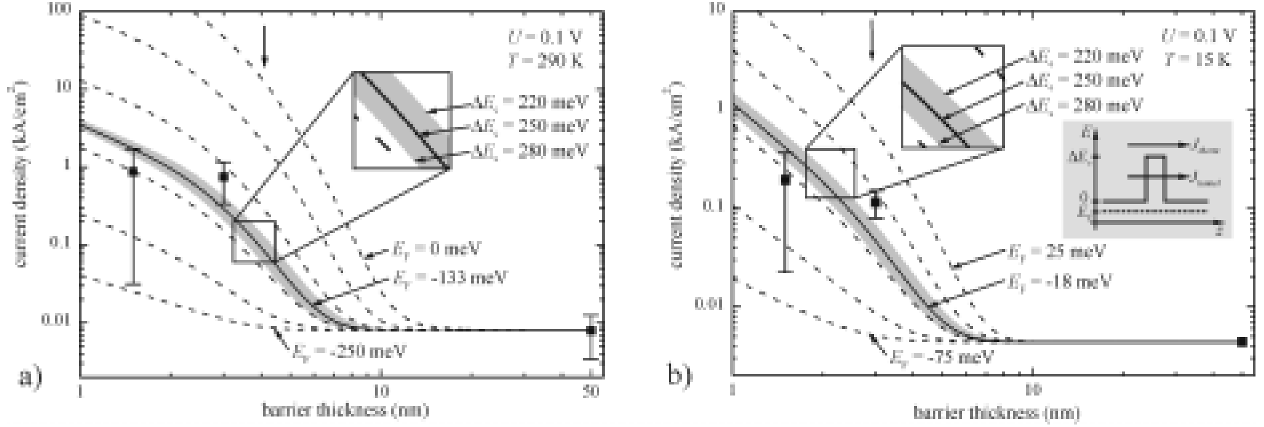

Figure 10. Calculated current-voltage-characteristics of InGaAs/InP/InGaAs-single barriers as a function of the barrier thickness with the Fermi energy E_F and the conductionband offset ΔE_c as parameters at 270 K (a) and 15 K (b); data points show experimental results.

There are two components contributing to the electron current. One part of the electrons tunnels through the barrier, the other one surmounts the potential barrier as a thermionic current J_{therm} according to the energetic distribution of electrons as described by the density-of-states function and the Fermi function. A schematic of this model is shown as an inset in Fig. 10 b), where ΔE_c is the conduction band offset between InGaAs and InP and E_F the Fermi energy. The total current density is given by

$$J_{total} = J_{therm} + J_{tunnel} \,. \qquad (1)$$

For given temperature and barrier height, J_{therm} does not change with varying barrier thickness whereas the tunneling current J_{tunnel} decreases with increasing thickness. Therefore, J_{therm} may be determined by measuring the current through a thick barrier – 50 nm in our case – where tunneling can be neglected. The tunneling current density can be calculated for low bias voltages after

$$J_{tunnel} = U \cdot \frac{2me^2}{\hbar^3} \cdot \int_0^{\Delta E_c} f(E, E_F) \cdot T(E) \,\mathrm{d}E \,, \qquad (2)$$

where m is the effective electron mass, e the elementary charge, and $\hbar$ Planck's constant devided by 2π[24]. $f(E,E_F)$ is the Fermi distribution in dependence on the electron energy E and the Fermi energy E_F. $T(E)$ is the transmission coefficient for a given potential barrier. U is the bias voltage (here: 0.1 V to ensure low-bias conditions).

In Fig. 10 the calculations are compared to data close to room temperature (a) and at 15 K (b). For thick barriers the total current amounts to the thermionic part and was set to the value measured with the 50 nm barrier. Reducing the thickness increases the tunneling current, where the position of the Fermi energy is found to be the most sensitive parameter. At a Fermi energy of 250 meV below the conduction band (E_F = -250 meV) only a small increase of the

current density is expected. If E_F equals the conduction band edge ($E_F = 0$ meV) a significant increase of the tunneling current is expected even for a barrier thickness of 10 nm. The best-fitting Fermi energy is drawn as bold line ($E_F = -133$ meV at 290 K and $E_F = -18$ meV at 15 K). This reflects the expected increase of the Fermi energy for lower temperatures[25]. At low temperatures the tunneling current is reduced as compared to room temperature due to the sharper Fermi distribution. The strong influence of the Fermi energy on the tunneling current offers the possibility to determine its value and/or the doping concentration in nano-heterostructures. The grey region around the bold lines of the best Fermi fit in Fig. 10 represents the current dependence on barrier height $\Delta E_c = 250 \pm 30$ meV. Its influence is clearly visible, but the influence of the Fermi energy is significantely higher. In order to estimate a barrier thickness below which tunneling dominates, we arbitrarily take that barrier where the corresponding current amounts ten times the thermionic current. Depending on the temperature this thickness is about 4 nm near room temperature (cf. arrow in Fig. 10 a) and about 3 nm at 15 K (cf. arrow in Fig. 10 b)). A compromise between electron tunneling and PL intensity concerning the optimum lower buffer layer thickness seems to be a thickness of nearly 5 nm.

5. CONCLUSION

Based on our previous QWR-laser concept we present a modified and optimized design. This includes an improved current confinement into the active region by inserting an additional current-blocking measure. This consists of an Al_2O_3 mask which is patterned in a self-aligning process. The parasitic upper InGaAsP-layer is removed during the same process and thus the emission from this region is effectively suppressed. Additionally, the upper InP buffer layer, which hampers the hole injection into the QWR, can be omitted, when the growth temperature of the QWR is increased to 640 °C. However, for lattice-matched QWRs the TMGa/TMIn ratio in the gasphase has to be increased as compared to growth at 600 °C. From tunneling experiments along with PL examinations we conclude that the optimum thickness of the lower InP buffer layer is about 5 nm.

ACKNOWLEDGEMENTS

The authors wish to thank N. Riedel and D. Rümmler for active technical support as well as N. Unger for assistance during optical and electrical measurements. The financial support of the Volkswagen-Stiftung and the Deutsche Forschungsgemeinschaft is gratefully acknowledged.

REFERENCES

1. B. A. Paldus, T. G. Spence, R. N. Zare, J. Oomens, F. J. M. Harren, D. H. Parker, C. Gmachl, F. Capasso, D. L. Sivco, J. N. Baillargeon, A. L. Hutchinson, and A. Y. Cho, "Photoacoustic spectroscopy using quantum-cascade lasers," *Optics Lett.*, **24**, pp. 178-180, 1999.
2. A. A. Kosterev, R. F. Curl, F. K. Tittel, C. Gmachl, F. Capasso, D. L. Sivco, J. N. Baillargeon, A. L. Hutchinson, and A. Y. Cho, "Effective utilization of quantum-cascade distributed-feedback lasers in absorption spectroscopy," *Appl. Optics*, **39**, pp. 4425-4430, 2000.
3. E. Kapon, "Quantum wire semiconductor lasers," in *Quantum Well Lasers*, P. S. Zory, ed., pp. 461-500, Academic Press, San Diego, 1993.
4. A. Yariv, "Scaling laws and minimum threshold currents for quantum-confined semiconductor lasers," *Appl. Phys. Lett.*, **53**, pp. 1033-1035, 1988.
5. Y. Arakawa, and H. Sakaki, "Multidimensional quantum well laser and temperature dependence of its threshold current," *Appl. Phys. Lett.*, **40**, pp. 939-941, 1982.
6. D. E. Wohlert, K. Y. Cheng, and S. T. Chou, "Temperature invariant lasing and gain spectra in self-assembled GaInAs quantum wire Fabry-Perot lasers," *Appl. Phys. Lett.*, **78**, pp. 1047-1049, 2001.
7. E. Kapon, D. M. Hwang, and R. Bhat, "Stimulated Emission in Semiconductor Quantum Wire Heterostructures," *Phys. Rev. Lett.*, **63**, pp. 430-433, 1989.
8. E. Kapon, "Quantum Wire and Quantum Dot Lasers," in *Semiconductor Lasers I: Fundamentals*, E. Kapon, ed., pp. 291-360, Academic Press, San Diego, 1998.
9. S. Tiwari, G. D. Pettit, K. R. Milkove, F. Legoues, R. J. Davis, and J. M. Woodall, "High efficiency and low threshold current strained V-groove quantum-wire lasers," *Appl. Phys. Lett.*, **64**, pp. 3536-3538, 1994.
10. T. G. Kim, K. H. Park, S.-M. Hwang, Y. Kim, E. K. Kim, S.-K. Min, S.-J. Leem, J.-I. Jeon, J.-H. Park, and W. S. Chang, "Performance of GaAs-AlGaAs V-Grooved Inner Stripe Quantum-Well Wire Lasers with Different Current Blocking Configurations," *IEEE J. Quantum Electron.*, **34**, pp. 1461-1468, 1998.

11. T. G. Kim, X.-L. Wang, Y. Suzuki, K. Komori, and M. Ogura, “Characteristics of the Ground-State Lasing Operation in V-Groove Quantum-Wire Lasers,” *IEEE J. Select. Top. Quantum Electron.*, **6**, pp. 511-521, 2000.
12. T. G. Kim, E. K. Kim, S.-K. Min, and J.-H. Park, “Improvement of carrier capture efficiency of short-period GaAs/AlGaAs quantum wire array by a new lithography method,”*Appl. Phys. Lett.*, **69**, pp. 955-956, 1996.
13. S. T. Chou, D. E. Wohlert, K. Y. Cheng, and K. C. Hsieh, “The directionality of quantum confinement on strain-induced quantum-wire lasers,” *J. Appl. Phys.*, **83**, 3469-3472, 1998.
14. T. Toda, and Y. Nakano, “Room Temperature Operation of 1.5 µm InAsP/InP Strained Quantum Wire DFB Lasers Fabricated by Mass Transport Method,” in *Proc. 11th Int. Conf. Indium Phosphide and Related Mater.*, Davos, Switzerland, May 16-20, pp. 17-20, 1999.
15. T. Schrimpf, P. Bönsch, D. Wüllner, H.-H. Wehmann, A. Schlachetzki, F. Bertram, T. Riemann, and J. Christen, “InGaAs quantum wires and wells on V-grooved InP substrates,” *J. Appl. Phys.*, **86**, pp. 5207-5214, 1999.
16. P. Bönsch, D. Wüllner, T. Schrimpf, A. Schlachetzki, and R. Lacmann, “Ultrasmooth V-Grooves in InP by Two-Step Wet Chemical Etching,” *J. Electrochem. Soc.*, **145**, pp. 1273-1276, 1998.
17. D. Piester, P. Bönsch, T. Schrimpf, H.-H. Wehmann, and A. Schlachetzki, “Laser-Action in V-Groove-Shaped InGaAs-InP Single Quantum Wires,” *IEEE J. Select. Top. Quantum Electron.*, **6**, pp. 522-527, 2000.
18. H.-H. Wehmann, T. Schrimpf, P. Bönsch, D. Wüllner, D. Piester, A. Schlachetzki, and R. Lacmann, “Growth and characterization of InGaAs quantum-wires,” in *Heterostructure Epitaxy and Devices - HEAD’97*, P. Kordos and J. Novak, eds., pp. 199-202, Kluwer Academic Publishers, Dordrecht, 1998.
19. T. Schrimpf, D. Piester, H.-H. Wehmann, P. Bönsch, D. Wüllner, A. Schlachetzki, C. Mendorf, and H. Lakner, “Preparation and characterization of InGaAs quantum wires on V-groove patterned InP,” in *Proc. 11th Int. Conf. Indium Phosphide and Related Mater.*, Davos, Switzerland, May 16-20, pp. 507-510, 1999.
20. D. Wüllner, A. Schlachetzki, P. Bönsch, H.-H. Wehmann, T. Schrimpf, R. Lacmann, and S. Kipp, “Characterization of quantum structures by atomic-force microscopy,” *Mater. Sci. Eng.*, **B 51**, pp. 178-187, 1998.
21. D. Wüllner, M. Chahoud, T. Schrimpf, P. Bönsch, H.-H. Wehmann, and A. Schlachetzki, “Diffusion during metalorganic vapor-phase epitaxy on V-groove patterned substrates,” *J. Appl. Phys.*, **85**, pp. 249-255, 1999.
22. P. Bönsch, D. Wüllner, T. Schrimpf, H.-H. Wehmann, and A. Schlachetzki, “Growth of InGaAs/InP quantum wires on patterned substrates, ” in *Proc. 7th Europ. Workshop Metal-Organic Vapour Phase Epitaxy and Related Growth Tech. (EW-MOVPE VII)*, Berlin, Germany, June 8-11, C1, 1997.
23. S. Adachi, “Chemical Etching of InP and InGaAsP/InP,” *J. Electrochem. Soc.*, **129**, pp. 609-613, 1982.
24. J. H. Davies, *The physics of low-dimensional semiconductors: an introduction*, Cambridge University Press, Cambridge, 1988.
25. P. S. Kirejew, *Physik der Halbleiter*, Akademie-Verlag, Berlin, 1974.